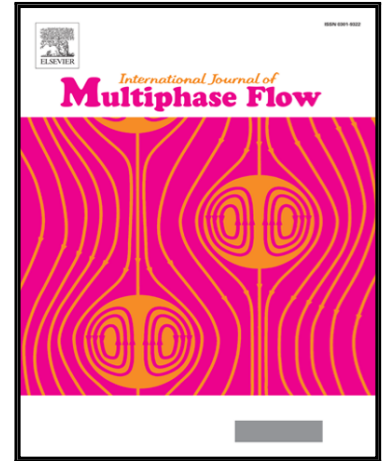


## Accepted Manuscript

### FLOW PATTERN TRANSITION IN LIQUID-LIQUID FLOWS WITH A TRANSVERSE CYLINDER

Maxime Chinaud , Kyeong Hyeon Park , Panagiota Angeli

PII: S0301-9322(16)30362-7  
DOI: [10.1016/j.ijmultiphaseflow.2016.11.011](https://doi.org/10.1016/j.ijmultiphaseflow.2016.11.011)  
Reference: IJMF 2511



To appear in: *International Journal of Multiphase Flow*

Received date: 24 June 2016  
Revised date: 21 October 2016  
Accepted date: 26 November 2016

Please cite this article as: Maxime Chinaud , Kyeong Hyeon Park , Panagiota Angeli , FLOW PATTERN TRANSITION IN LIQUID-LIQUID FLOWS WITH A TRANSVERSE CYLINDER, *International Journal of Multiphase Flow* (2016), doi: [10.1016/j.ijmultiphaseflow.2016.11.011](https://doi.org/10.1016/j.ijmultiphaseflow.2016.11.011)

This is a PDF file of an unedited manuscript that has been accepted for publication. As a service to our customers we are providing this early version of the manuscript. The manuscript will undergo copyediting, typesetting, and review of the resulting proof before it is published in its final form. Please note that during the production process errors may be discovered which could affect the content, and all legal disclaimers that apply to the journal pertain.

**Highlights**

- Novel way to actuate transition from stratified to dispersed liquid-liquid flows.
- Presence of bluff body to localise wave generation in stratified liquid-liquid flows.
- High speed PIV is used to study flow fields in liquid-liquid flows.
- Interfacial waves downstream a bluff body have same frequency as von Karman vortices.

ACCEPTED MANUSCRIPT

## FLOW PATTERN TRANSITION IN LIQUID-LIQUID FLOWS WITH A TRANSVERSE CYLINDER

Maxime Chinaud, Kyeong Hyeon Park, Panagiota Angeli\*

Department of Chemical Engineering, University College London, London WC1E 7JE, UK

\*Corresponding author: Email: p.angeli@ucl.ac.uk, Tel:+44 (0) 20 7679 3832

### Abstract

The effect of a cylindrical bluff body on the interface characteristics of stratified two-phase, oil-water, pipe flows is experimentally investigated with high speed Particle Image Velocimetry (PIV). The motivation was to study the feasibility of flow pattern map actuation by using a transverse cylinder immersed in water in the stratified pattern, and particularly the transition from separated to dispersed flows. The cylinder has a diameter of 5 mm and is located at 6.75 mm from the pipe top in a 37 mm ID acrylic test section. Velocity profiles were obtained in the middle plane of the pipe. For reference, single phase flows were also investigated for Reynolds numbers from 1550 to 3488. It was found that the flow behind the cylinder was similar to the two dimensional cases, while the presence of the lower pipe wall diverted the vorticity layers towards the top. In two-phase flows, the Froude number (from 1.4 to 1.8) and the depth of the cylinder submergence below the interface affected the generation of waves. For high Froude numbers and low depths of submergence the counter rotating von Karman vortices generated by the cylinder interacted with the interface. In this case, the vorticity clusters from the top of the cylinder were seen to attach at the wave crests. At high depths of submergence, a jet like flow appeared between the top of the cylinder and the interface. High speed imaging revealed that the presence of the cylinder reduced to lower mixture velocities the transition from separated to dual continuous flows where drops of one phase appear into the other.

*Key words:* oil-water flow; bluff body; stratified flow; dispersed flow; PIV measurements; flow pattern map actuation

## 1. Introduction

Two phase flows in pipes (gas-liquid and liquid-liquid) have been studied extensively both experimentally and theoretically, because of the wide range of applications including oil and gas transportation, evaporation and condensation systems, two phase reactions and separations. The studies in their majority deal with gas-liquid systems and free surface flows. The large density and viscosity ratios, as well as the limited range of surface tension values encountered in gas-liquid flows allow certain simplifications that enable the development of models for predicting their hydrodynamic behaviour (Taitel & Dukler, 1976; Barnea & Taitel, 1994; Taitel & Barnea, 1990). These models, however, may not be suitable for liquid-liquid systems. Initial studies on liquid-liquid flows produced flow pattern maps and empirical correlations for the prediction of pressure drop. Many current efforts focus on the detailed measurements of local flow parameters, such as interfacial wave characteristics, drop sizes and phase distribution (Barral & Angeli, 2013; Morgan et al, 2013; Hu & Angeli, 2006; Simmons & Azzopardi, 2001; Hu et al., 2006). The flow pattern transitions depend on the flowrates and properties of the phases, the pipe size and inclination and have been attributed to many different physical mechanisms (e.g. Brauner & Moalem-Maron, 1993; 1991).

An important transition is from stratified flows, where a well-defined interface separates the two continuous liquid layers, to dispersed flows, where drops of one or both phases form into the other. Two different theoretical approaches have been used to predict the boundary between stratified and dispersed flows. In one approach the stability analysis of the momentum balance equations with appropriate closure relations is studied (Lin & Hanratty, 1987; Brauner & Moalem-Maron, 1992). The transition is then considered to happen when a disturbance on the interface in stratified flows, induced by Kelvin-Helmholtz instabilities, is amplified. In the other approach, the balance of forces such as gravity, surface tension, drag force and pressure difference, is considered. From the interfacial waves drops will eventually detach, which signify the transition to dispersed patterns (Al-Wahaibi & Angeli, 2007; Ishii & Grolmes, 1975).

Experimentally it is challenging to study flow pattern changes because of the transient nature of the flow and uncertainty in their occurrence. The study of the transition from separated to dispersed flows would entail capture of the first drops that detach from the interface at some unknown location in the pipe. At the beginning of the transition the drop detachment occurrences are very few which makes their study even more difficult. A novel approach to study flow pattern transitions is to actuate the changes. This would facilitate their study as the transition can be controlled and localised and can find industrial applications in the cases where certain patterns are desirable.

One way to force a transition in the flow pattern map is to generate shear flow by using a bluff body. This approach is common in the naval industry where hydrofoils are used to disperse bubbles in water and reduce drag (up to 15% for Lin & Rockwell, 1995; Duncan & Dimas, 1996). When a hydrofoil is submerged in water, the flow disturbances generated in the wake of the bluff body interact with the free surface and generate bubbles. Despite their extensive use by industry, hydrofoils have complicated geometry, which does not allow theoretical analysis of the flow. For this reason, most of the investigations dealing with a submerged body beneath a free surface have used cylinders instead. In liquid-liquid flows the first study, which demonstrated that a cylinder inside a pipe actuates the flow pattern map, was published by Park et al. (2016). The results showed that the presence of the bluff body generated waves at the oil-water interface in stratified flows and shifted the transition from stratified to dispersed patterns to lower mixture velocities. In the work by Park et al. (2016), however, only high speed imaging was used to study the interfacial waves. It was not possible therefore to directly link any flow structures generated by the bluff body to changes in interfacial configuration.

The studies on the interaction of a bluff body with fluids which are relevant here, can mainly be categorised into two fields. The first field considers the interaction of a free surface flow past a bluff body, while the second considers flow past a bluff body in the presence of a solid wall. In the studies with free surface flows behind a cylinder solid boundaries are not considered (assumption of deep water) and Reynolds numbers of the order of magnitude of 1000 have been used. Large scale structures, von Karman vortices, are emitted in the wake of the cylinder with a well-defined frequency. The interface motion and the droplet detachment mainly depend on the depth of submergence of the cylinder from the free surface and the Froude number. Theoretical analysis and numerical simulations for the 2D problem show that for large depths of submergence and low Froude numbers, the interface propagates as a

classical gravity wave with small amplitude. However, even for large depths of submergence induced interfacial waves are still observed with increasing Froude number, which may lead to droplet detachment (Triantafyllou & Dimas, 1989; Dimas, 1998).

Velocity fields downstream a submerged cylinder have been obtained both experimentally and numerically which revealed different hydrodynamic patterns and corresponding interface motion that depended on the Froude number and depth of submergence (Sheridan et al., 1997; Reichl et al., 2005). The presence of a free surface close to the submerged cylinder modified the von Karman vortex structure; a jet like-flow developed above the cylinder which, for some conditions, attached to the interface and generated disturbances (wave motion). Sheridan et al. (1997) have pointed out the crucial role of the jet like-flow attachment/detachment on the interface and on the breaking waves and droplet detachment.

For the actuation of flow regime transition in pipe flows the solid wall boundaries need to be considered as well. The effect of walls on the flow behind a transverse cylinder has been studied both experimentally and numerically (Wang & Tan, 2007; Zovatto & Pedrizzetti, 2001; Ding et al, 2004). To the best of our knowledge, all studies available have been conducted in rectangular tanks where the third dimension is neglected. For a cylinder placed between two solid boundaries the *blockage ratio*, defined as the ratio between the cylinder diameter and the distance between the two walls, can affect the flow (Chen et al, 1995). It has been found, however, that no significant changes in the hydrodynamic patterns behind the cylinder can be observed for blockage ratios below 0.5. Another important parameter in confined flows is the *gap ratio*, defined as the distance from the wall to the bottom of the cylinder over the cylinder diameter. Below a critical gap ratio the flow is blocked beneath the cylinder. In such cases the cylinder acts like a surface-mounted obstacle where the coupling of the wall and the cylinder vorticity layers suppresses the vortex periodic shedding (Lei et al, 1999). Zovatto & Pedrizzetti (2001) estimated the critical gap ratio from numerical simulations in 2D single phase flows to be around 0.3. They also found that the presence of a wall close to the cylinder disturbed the large scale vortical structures and induced asymmetry to the vorticity contours. In general, the presence of the wall did not affect significantly the vortex shedding frequency and the Strouhal number was about 0.2, similar to unbounded flows (Bearman & Zdravkovich, 1978; Choi & Lee, 2000). However, at gap ratios lower than 0.25 the Strouhal number was found to be higher and equal to 0.4 (Grass et al, 1984). These values seem to represent a transitional regime between non-disturbed vortex shedding and blockage characterized by the absence of any vortex shedding.

The numerical or theoretical studies available on the effect of a rigid wall on the vortex shedding behind a cylinder are generally considering 2D configurations (Wang and Tan, 2008; Ding et al, 2004; Lin et al, 2009). In pipe flow, 3D effects can become predominant. A further assumption generally used in the literature is that the incoming interface approaching the cylinder is flat.

The aim of the current work is to study experimentally the effect of a transverse cylinder on stratified liquid-liquid pipe flows. In a previous paper by Park et al. (2016), it was shown that interfacial waves were generated when a cylinder was present in stratified oil-water flows. These waves had frequencies which gave Strouhal number equal to 0.2, as expected for von Karman vortices behind a bluff body and were different from the frequencies measured when the bluff body was not present (frequencies were constant and close to 20 Hz). To be able to directly link however, the interfacial waves with the presence of the bluff body it is important to study the velocity fields downstream the cylinder and obtain the structure of the vortices generated by the bluff body. Velocity fields will be investigated with Particle Image Velocimetry (PIV).

PIV techniques have been extensively used in the two last decades to obtain velocity fields in a variety of flow configurations (Adrian and Westerweel, 2011; Raffel et al, 2013): In large scale flows, tracer particles are introduced in the fluid studied and illuminated by a laser light sheet which defines the plane of measurement. From consecutive images of the tracers, velocity fields are obtained via cross correlation. The accuracy of the PIV measurements is of the order of 0.05 pixel (Stanislas et al, 2008) and is limited by the variation of particle image intensity (Nobach & Bodenschatz, 2009). Errors in PIV can arise for example from particle image size, gradients inside the correlation box, and their quantification is still an active research field (Wieneke, 2015; Charonko and Vlachos, 2013; Sciacchitano et al, 2013). The PIV studies on liquid-liquid stratified flows in pipes are limited (Morgan et al, 2013; Kumara et al, 2010). In stratified two phase flows in general, light is reflected from the interface especially when it is very wavy, which can decrease the accuracy of the PIV measurements in its vicinity. Techniques that have been developed to overcome this generally involve complicated PIV codes or measurement set ups (Theunissen et al 2008; Birvalski et al, 2014, Zhou et al, 2015; Cheng et al, 2015).

In what follows, the experimental facilities, the location of the cylinder in the pipe and the PIV measurements are described first. Single phase flow results are then presented and the effects of wall boundaries on the hydrodynamics of the large scale vortices are discussed.

These are followed by the two-phase flow studies; these studies are limited to linear waves where PIV measurements are possible close to the interface. Finally, results on droplet detachment from the actuated waves are discussed.

## 2. Experimental setup

The experiments were conducted in the two phase oil-water flow facility located in the Dept of Chemical Engineering, UCL. The facility is a closed loop system and has an acrylic test section with 37 mm ID and about 8 m length. The two fluids are separately pumped from their respective storage tanks by two centrifugal pumps. The flowrate of each fluid is controlled via a recycle line and measured with a flowmeter (ABB Instrumentation Ltd) with accuracy of 1% full range and range between 20 L min<sup>-1</sup> and 250 L min<sup>-1</sup>. The fluids join at a symmetric Y-shaped junction at the test section inlet. After the test section, the two fluids are led to a separator equipped with a KnitMesh<sup>TM</sup> coalescer that facilitates the separation of the two phases. The organic and the aqueous phases are then returned from the top and the bottom of the separator respectively into their storage tanks (Barral & Angeli, 2013). The test fluids used for this study are water (density  $\rho = 1000 \text{ kg m}^{-3}$  and viscosity  $\mu = 0.001 \text{ kg m}^{-1}\text{s}^{-1}$ ) and Exxsol D140 oil ( $\rho = 830 \text{ kg m}^{-3}$  and  $\mu = 0.0055 \text{ kg m}^{-1}\text{s}^{-1}$ ). The Y-junction has branches with diameter equal to the main test section diameter; according to their density, oil is introduced from the top branch and water from the bottom one. A transverse cylinder with 5 mm OD is placed 460 mm after the Y-junction across the direction of the flow (Park et al., 2016). This distance was chosen considering mainly two things. Locating the rod close to the inlet allows maximum downstream test section length for the studies of flow pattern changes. Previous single phase PIV measurements without the rod showed that the flow was already fully developed at this distance. In addition, it was found that Kelvin-Helmholtz waves forming after the Y-inlet are mainly smooth and two dimensional for a short distance but then develop 3D fluctuations (Park et al., 2016). Positioning the rod close to the inlet ensured that only smooth waves interacted with the rod, which is easier to study with PIV.

The two phase flow experiments were carried out for oil and water flowrates varying independently at 20, 25, 30 L min<sup>-1</sup>. For these flowrate combinations the pattern was stratified or stratified wavy when the bluff body was not present. In the presence of the bluff body the interface upstream the cylinder was either flat or had smooth waves. Combining these flowrates provides six different case studies. To characterize the two phase flow in the pipe,

the mixture velocity,  $U_{\text{mix}}$ , and the oil-to-water flowrate ratio,  $r$ , will be used, defined as follows:

$$U_{\text{mix}} = \frac{Q_o + Q_w}{\pi R^2}, \quad (1)$$

$$r = \frac{Q_o}{Q_w}. \quad (2)$$

where  $R$  corresponds to the radius of the test section, and  $Q_o$  and  $Q_w$  are the oil and water flowrates respectively. The position of the transverse cylinder inside the pipe and relative to the interface is important. To study the interaction between the interface and the vortices generated by the cylinder, there should be no direct impact of the incoming interface with the cylinder which can break the interface.

As discussed in the Introduction, the depth,  $h$ , of the cylinder submergence below the interface (see Figure 1) and the Froude number determine the interactions between the flow generated in the wake of the cylinder and the interface. The interface height and therefore the depth of submergence depend on the ratio  $r$  of the oil and water flowrates:

$$h(r), \quad (3)$$

while the Froude number can be calculated as follows:

$$Fr = \frac{U_{\text{mix}}}{\sqrt{gd}} = \frac{1}{\pi R^2 \sqrt{gd}} (Q_w + Q_o), \quad (4)$$

where  $g$  and  $d$  are respectively the acceleration of gravity and the diameter of the transverse cylinder. Generally, in the computation of the Froude number the mean velocity of the incoming water flow is used (Triantafyllou & Dimas, 1989; Dimas, 1997, Sheridan et al, 1997; Reichl et al, 2005). In the previous studies, however, either numerical or experimental in open water tanks, the water velocity and the depth of submergence could be varied independently. In the case of stratified liquid-liquid flows in a pipe, the interface height depends in a non-linear way on the flowrates of the two phases. As a result, the interface height and the in-situ water velocity, or the depth of submergence and the Froude number based on water velocity, cannot be varied independently. Since the water velocity is not known beforehand, for convenience, it was decided to define the Froude number using the mixture velocity, which is an input parameter. In two-phase flows, the flow pattern maps are usually plotted in terms of mixture velocity against phase volume fraction (or flowrate ratio); the Froude number and the depth of submergence, related to the mixture velocity and the flowrate ratio, can therefore be considered as alternative parameters in the flow pattern maps. For flow rate ratios different to one, the interface is wavy mainly due to the Kelvin-Helmholtz instabilities (Funada & Joseph, 2001) which make difficult the definition of the depth of

submergence. For such cases, the mean average of the incoming wavy interface will be considered. The transverse cylinder was placed approximately 6.75 mm above the bottom of the pipe (Figure 1). For the flowrate combinations considered this gave depths of submergence between 5 and 15 mm, while there was no direct impact of the incoming interface to the cylinder. A summary of the experimental conditions studied for both single and two phase flows can be found in Table 1. The Reynolds numbers based on both the cylinder diameter ( $Re_{cyl}$ ) and on the pipe diameter ( $Re_{pipe}$ ) have also been calculated. For the two phase experiments, the Reynolds numbers have been computed based on the water phase velocity. The mean water phase velocity has been calculated by divided the water flow rate by the cross sectional area occupied by the water phase  $S_W = \pi R^2 \left( \frac{Q_W}{Q_W + Q_O} \right)$ .

The velocity profiles in the water phase were studied downstream the transverse cylinder with high speed Particle Image Velocimetry (PIV). For these measurements, water was seeded with silver coated hollow glass particles with 10  $\mu\text{m}$  diameter (Litron Lasers, Ltd). A double pulsed Nd-YAG Laser (TSI instruments) with 532 nm wavelength was used to illuminate the flow from underneath the pipe. The light sheet was generated using a classical expanded laser beam optical system (Adrian & Westerweel, 2011). Optical lenses were arranged so that the laser sheet was vertical in the middle of the pipe section along the pipe axis. As was discussed above only flowrate combinations which resulted in relatively smooth interfaces were considered to avoid optical distortions close to the interface. The estimated laser sheet thickness was about 1 mm. The typical curvature of the interface in the transverse direction is estimated to be on the order of 10 mm. Consequently the optical distortion from the curvature of the interface in the transverse direction can be neglected. Further optical distortions at the interface are avoided as the laser plane enters in the water phase. Images were recorded with a high speed camera (Photron SA-1) with 1024 $\times$ 1024 pixels in full field and 12-Bits greyscale. The camera was located perpendicular to the laser sheet and was equipped with a 105 mm Nikon lens. To avoid refractive distortions, an acrylic box filled with glycerol was used around the part of the test section where the measurements were taken (Prasad, 2000). In high speed PIV the acquisition frequency of the camera is set to twice the frequency of the laser pulse emitted by each of the laser cavities. The time separating two consecutive image pairs defines the time separating two consecutive velocity fields. The corresponding  $\delta t$ , the time separating two consecutive images, is therefore, equal to the inverse of the camera acquisition frequency. For the same image magnification and spatial resolution, the sampling frequency in the PIV measurements varied depending on the flowrates. The maximum image acquisition

frequency corresponding to the minimum  $\delta t$  was 3 kHz (i.e.  $\delta t = 0.333$  ms). Image acquisition was triggered by the laser pulse using a synchronizer (TSI Instruments). Data was logged in a computer where the 2D velocity fields were calculated with Insight4G (TSI, instruments). The pixel size was  $\delta = 94$   $\mu\text{m}$  and velocity fields were computed using a  $32 \times 32$  pixel correlation box with 50% spatial overlapping which gives a spatial resolution for the velocity vectors of 1.5 mm. The range of velocity measurable depends on the inverse of the frequency of the camera. For each flow condition we fixed the maximum velocity magnitude to correspond to the half part of the correlation box. Consequently, the range of velocity magnitudes (which depends on  $\delta t$ ) was from 1 pixel/  $\delta t$  to 16 pixels/  $\delta t$ . For each set of conditions from 200 to 1000 images were acquired.

### 3. Results

#### 3.1 Single phase flow

Wang and Tan (2008) have produced a review of experimental work of the last three decades, on the effect on flow of a completely submerged cylinder in the presence of a rigid boundary. As discussed in the Introduction, there are no studies on the flow behind a cylinder within a pipe. For this reason experiments were carried out initially to characterise the single phase flow features. Six different water velocities were considered corresponding to Reynolds numbers from 1555 to 3448. The Reynolds number has been computed based on the transverse cylinder diameter and corresponding velocity. The blockage ratio (i.e. the ratio between the cylinder diameter and the pipe diameter) has been fixed at 0.13 which is below the critical value of 0.5 suggested by Chen et al. (1995). The gap ratio,  $\gamma$  (defined as  $\gamma = H/d$ , where  $H$  is the distance from the wall to the bottom of the cylinder) varies along the transverse direction because of the pipe curvature. Taken at the pipe centre,  $\gamma(z = 0) = \frac{6.75}{5} = 1.35$ , which is larger than the critical value of 0.3 where the flow underneath the cylinder is affected from the presence of the wall (Zovatto and Pedrizetti, 2001). This value will decrease closer to the pipe wall along the transverse axis. The gap ratio becomes equal to 0.3 at  $z = \pm 138$  mm. The curvature of the pipe along the transverse direction will still affect the flow behind the cylinder but it can be assumed that the gap will only become significant close to the pipe wall and would have a small effect on vortex shedding frequency in the observation plane in the middle of the pipe.

In the PIV measurements it was possible to correlate successive images which suggests that the z-axis velocity component is weak enough so that the particle tracers remain in the observation plane (i.e. laser sheet) during the time of measurement.

The introduction of the bluff body in single phase flow generates a shear zone in the wake of the cylinder. This is demonstrated in Figure 2 where the average velocity profiles in a vertical pipe diameter are shown. The shear zones shown in the different profiles generate the shedding of counter rotating vortices; this is in agreement with literature as the Reynolds numbers investigated are above the critical value ( $Re = 100$ ) for vortex shedding (Zovatto and Pedrizzetti, 2001). The profiles however, exhibit different behaviour depending on the distance downstream the cylinder. Figure 2a shows the velocity profiles averaged over time and over the distance from  $3d$  to  $14d$  (i.e. 20 mm to 40 mm after the cylinder). The velocity is high at the upper part of the pipe and decreases as the cylinder is approached, before increasing again below the cylinder. The highest shear zones are located on the wall boundaries and on the top and the bottom part of the cylinder. The stratification in the velocity profile along the radial distance increases with the Reynolds number as expected.

The same velocity profiles normalised by the maximum velocity value, have also been plotted in the vicinity of the cylinder (0 to  $2d$  or from 0 to 10 mm after the cylinder) in Figure 2b but for the lower part of the pipe. The velocity profile shapes are comparable to those reported by Wang and Tan (2008) for gap ratios above 0.4, even though these were obtained in a rectangular tank at different gap ratios and Reynolds numbers. In both cases the normalized velocity profiles are symmetric with maximum values above and below the cylinder and a minimum value at location of the centre of the cylinder. Wang and Tang (2008) reported an asymmetry in the velocity profile in the vicinity of the cylinder for low gap ratios, which however, decreased with increasing ratio. The shapes of the velocity profiles, shown in Figure 2b, are independent of the Reynolds number and clearly show that they are similar in the two regions above and below the cylinder. It appears that the pipe geometry and the chosen gap ratio do not disturb the vortex generation mechanisms in the wake immediately downstream the cylinder. For a better visualization of the spatial stratification of the velocity in the central plane of the pipe, time averaged axial velocity fields normalized by the corresponding  $U_{mix}$  are shown in Figure 3 for two different Reynolds numbers. The flow features do not change within the range of Reynolds numbers investigated while the velocity stratification is more pronounced at the high Reynolds number. Three different regions in the wake of the cylinder can be defined. The first one, located between axial distances 0 and  $2d$  (from 0 to 10 mm after the cylinder) corresponds to the velocity profiles shown in Figure.2.b. This region exhibits

two high magnitude time averaged velocity lobes located on the top and the bottom of the cylinder. These lobes show a high degree of symmetry along the radial direction but not along the axial one. Indeed, the high magnitude velocity lobe located on the bottom of the cylinder seems to be more elongated along the direction of the flow. In this region, the shear flow exhibits the initial mechanism of counter vortex generation. The extended bottom velocity lobe indicates that the vortex street will be slightly shifted to the top of the pipe. At axial distances between  $2d$  to  $6d$  (from 10 to 30 mm after the cylinder), the second transitional region occurs. The time averaged axial velocity lobe located on the bottom of the cylinder tends to decrease along the direction of the flow. The third region appears at axial distances greater than  $6d$ . In this region, the flow is divided in two parts, a low velocity magnitude one at the lower part of the pipe and a high velocity magnitude one at the upper part of the pipe, above the cylinder. In this region, far from the cylinder, the large scale vortices are advected along the flow direction. The lower mean velocity magnitude area corresponds to the zone in which the vortices are travelling; indeed the recirculation of the vortices decreases the time averaged velocity magnitude. As can be seen, in the third region the isocontours of the time averaged axial velocity field are not parallel to the flow but slightly inclined to the upper part of the cylinder indicating that the vortex street is shifted to the top of the pipe.

The vortex shedding frequency,  $f$ , is generally studied by computing the non-dimensional Strouhal number,  $St = \frac{fd}{U_s}$  where  $U_s$  represents the fluid superficial velocity. The variation of the Strouhal number with Reynolds number is shown in Figure 4. The different frequencies have been computed by plotting the FFT of the radial velocity component fluctuations at a distance  $8d$  downstream the cylinder and at the same height as the centre of the transverse cylinder. The Strouhal number does not vary significantly in the range of the investigated Reynolds numbers and is approximately equal to 0.21 which is similar to values reported in the literature for unbounded flows. The presence of the pipe wall underneath the cylinder clearly does not affect the vortex shedding frequency for the gap ratios investigated. This is in agreement with studies in rectangular channels (Wan and Tan, 2008) for similar Reynolds numbers.

To evaluate the effect of the wall on the vortical structures behind the cylinder the spanwise vorticity component was calculated as follows:

$$\omega_z = \frac{\partial V}{\partial x} - \frac{\partial U}{\partial y}, \quad (5)$$

where  $U$  and  $V$  represent respectively the horizontal and the vertical velocity components. Figure 5 shows the time averaged spanwise vorticity component for two different Reynolds

numbers. The main vorticity structures appear, as expected, on the top and the bottom of the cylinder. Increasing the Reynolds number tends to decrease the size of the two vorticity lobes, while a reattachment on the cylinder base of these two lobes is also seen. The corresponding Reynolds stresses are also plotted in Figure 6. The Reynolds stresses are computed from the product  $u'v'$ . The velocity fluctuations are found from  $u' = U - U_m$  and  $v' = V - V_m$  where  $U_m$  and  $V_m$  are respectively the time averaged horizontal and vertical velocity components. The Reynolds stresses are localized on the wake of the cylinder and concentrate in two opposite regions. The positive region is at the low part of the flow while the negative region is at the top. The results are qualitatively comparable to those obtained in rectangular channels. The pattern is almost symmetric at the low Re. In addition, at this Re two small clusters of Reynolds stresses appear upstream the main clusters with opposite signs to them (Figure 6a). The pattern becomes less symmetric as Re increases (Figure 6b). The positive Reynolds stress region becomes more predominant and tends to shift the low Reynolds stress region to the top of the pipe. The shear layer at the bottom wall interacts with the positive lobe of the Reynolds stresses and pushes the clusters of  $u'v'$  to the upper part of the pipe. These results, consistent with the time averaged velocity field maps displayed in Figure 3, indicate that the vortex street is shifted to the top of the pipe with increasing Reynolds number. In previous studies the loss of symmetry in Reynolds stresses occurred with decreasing gap ratio (Wang & Tan, 2008).

It should be mentioned that the results shown in Figures 5 and 6 were obtained by increasing the spatial resolution of the high speed PIV images. To capture the vortical flow structures very near the cylinder, the spatial resolution needs to be high. This is possible since the velocity magnitude in the direct wake of the cylinder is lower than in the rest of the pipe, e.g. the velocity in the upper part of the pipe can be two times higher than in the wake of the cylinder (see Figure 2).

The vorticity calculated from equation 5 contains the effects of both shear action and swirling (Zovatto and Pedrizetti, 2001). The shear layers corresponding to the bottom part of the pipe and the wake of the cylinder represent the main vorticity regions but do not necessarily generate vortices. Indeed, vorticity due to shear stresses can fail to track vortex structures. Vortex tracking has been discussed previously by Jeong and Hussain (1995) who proposed the parameter  $\lambda_2$  (Eq. 6) to discriminate the shearing and the swirling regions of vorticity.

$$\lambda_2 = \left( \frac{\partial U}{\partial x} + \frac{\partial V}{\partial y} \right)^2 - 4 \left( \frac{\partial U}{\partial x} \frac{\partial V}{\partial y} - \frac{\partial U}{\partial y} \frac{\partial V}{\partial x} \right) \quad (6)$$

For vorticity generated by shearing action,  $\lambda_2$  is positive, while for vorticity generated by swirling,  $\lambda_2$  is negative. Figures 7 and 8 shows the time sequence of  $\lambda_2$  for the two Reynolds numbers shown in the previous figures with the corresponding velocity fields superimposed. The time delay between each image is 20 ms for  $Re=1550$  (Figure 7) and 10 ms for  $Re=3488$  (Figure 8). As can be seen at these conditions the value of  $\lambda_2$  in the pipe is either zero or positive. The cylinder mainly generates shearing regions which are advected downstream at different velocities. With increasing Reynolds number the velocity in the shearing regions increases as well. In addition, the increase in  $Re$  tends to spread the shearing region in the pipe. In both cases, the lower pipe wall shifts the vorticity structures to the top. This is more pronounced for the high  $Re$  where at distance  $14d$  (i.e. 70 mm) downstream the cylinder, the shearing regions can go up to 5 mm above the centre of the pipe, while at low  $Re$  they do not reach the pipe centre.

The single phase flow studies indicate that the 3D pipe geometry does not affect significantly the flow features behind the cylinder in the central plane of the pipe, compared to the previous experimental studies in rectangular channels. In addition, the bottom pipe wall clearly interacts with the flow in the wake of the cylinder.

### 3.2 Two phase flow

In the two-phase flow cases it is important to capture the interface shape. Previously, for cases when the refractive index between the two liquid phases was matched, a very small quantity of fluorescent particles was injected close to the interface, which made the interface to appear as a bright line (Mohamed-Kassim & Longmire, 2004). In another approach, used in gas-liquid flows, a second camera, slightly inclined to the horizontal direction of the flow and simultaneously triggered with the PIV camera, was used to capture the shape of the waves (Birvalski et al, 2014). In the present study, the interface was detected from the signal of the seed particles in the water phase. The signal of the particles was increased and blurred and the contour of the seeded phase was then obtained by binarising the image obtained. To remove any optical artefacts near the interface due to reflections or the presence of any droplets, the binary image was eroded by following a 9-pixel connectivity criterion (Chinaud et al, 2015).

The two-phase flow PIV measurements were carried out in stratified and stratified wavy flows characterised by linear waves. Both the effect of Froude number and cylinder submergence (which depends on the ratio of the flowrates) were investigated. The Froude number varied from 1.4 to 1.8 (based on mixture velocity), which correspond to oil/water flow rates from 20

to  $30 \text{ L min}^{-1}$ . The effect of the Froude number on wave motion can be seen in Figure 9 for equal phase flow rates ( $r = 1$ ) for two cases,  $Fr = 1.4$  and  $1.8$ . The time averaged interface shape has been superimposed as a dark line on the 200 interface shapes obtained over time. In both cases, the time averaged interface shape is almost flat. The interface height for these flow conditions is expected to be in the middle of the pipe when no cylinder is present (Barral & Angeli, 2013). The difference in the interface height from the middle position is attributed to the hydraulic jump induced by the cylinder. As can be seen, the interface fluctuations increase with the Froude number. From the interface shapes over time the velocities of the waves can be obtained with cross correlation. It was found that the wave velocities were lower than the mixture velocity,  $U_{\text{mix}}$ . For the cases shown in Figure 9 the wave velocities are around  $0.42 \text{ m/s}$  for  $Fr=1.4$  and  $0.69 \text{ m/s}$  for  $Fr=1.8$  while the  $U_{\text{mix}}$  are  $0.62 \text{ m/s}$  and  $0.77 \text{ m/s}$  respectively. The frequencies of the waves, obtained with FFT computation, were found to be around  $18 \text{ Hz}$  (for  $Fr=1.4$ ) and  $35 \text{ Hz}$  (for  $Fr=1.8$ ) which give a Strouhal number of about  $0.2$ , the values expected for vortices shed by unbounded cylinders in single phase flows. It should be noted that the FFT resolution is not very high because the high sampling frequency of the camera (between  $750$  and  $1500 \text{ Hz}$ ) allows measurements for a short time when, depending on the frequency, from  $200$  to  $1000$  images can be collected.

The effect on wave motion of the depth of the cylinder submergence below the interface can be seen in Figure 10 for two symmetric cases,  $Q_o = 30 \text{ L min}^{-1}$  and  $Q_w = 20 \text{ L min}^{-1}$  ( $r = 1.5$ , Figure 10a) and  $Q_o = 20 \text{ L min}^{-1}$  and  $Q_w = 30 \text{ L min}^{-1}$  ( $r = 0.66$ , Figure 10b) and Froude numbers equal to  $1.8$ . For oil-to-water flowrate ratio  $r = 1.5$  (Figure 10a), the time averaged interface shape is centred just below the middle plane of the pipe. The wave amplitudes grow significantly downstream the bluff body. At a distance corresponding to  $8d$  ( $40 \text{ mm}$  from the cylinder) the amplitude has reached the highest value observed in this study, equal to  $\pm 5 \text{ mm}$ . For flow rate ratio above one (Figure 10b), the mean position of the time averaged interface shape is above the middle of the pipe and the amplitude of the waves is less. The presence of the bluff body tends to increase the mean interface height compared to flows without the cylinder. These results are in agreement with the previous studies in the same facility on wave formation using a bluff body for a wider range of flowrates (Park et al 2016). Wave velocities and frequencies are similar however, in both cases. The computed velocities are  $0.8 \text{ m/s}$  for  $r=1.5$  and  $0.77 \text{ m/s}$  for  $r=0.66$ , while in both cases the main FFT peak is at  $29 \text{ Hz}$ , which gives a Strouhal number equal to  $0.2$ . In the range of flowrates investigated, the effect of bluff body submergence on wave generation is more pronounced than that of Froude number.

The wave frequencies were compared with the frequencies of von Karman vortices downstream the cylinder, which were calculated from the FFT of the fluctuations of the vertical velocity component. The results showed that these frequencies matched and the von Karman vortices appear to “print their frequency on the interface. Velocity fields are presented below for indicative cases to further how the vortices interact with the interface.

The evolution of the velocity fields over time is shown in Figures 11 and 12 for the flowrate combinations  $Q_o=30 \text{ L min}^{-1}$ ,  $Q_w=20 \text{ L min}^{-1}$  ( $r=1.5$ ,  $Fr=1.8$ ) and  $Q_o=20 \text{ L min}^{-1}$ ,  $Q_w=20 \text{ L min}^{-1}$  ( $r=1$ ,  $Fr=1.4$ ) respectively. These two cases correspond to the most pronounced wave actuation and to an almost flat interface. For both figures the time difference between images is 6.7 ms. To observe the recirculation patterns in the water phase the velocity of the wave has been subtracted from the water phase axial velocity component. As can be seen in Figure 11, the vortices generated on the top of the cylinder are directly in contact with the interface and actuate it by increasing the amplitude of the waves. The shear layer generated at the bottom boundary of the pipe, as shown in single phase flow (see previous section), seems to advect the vorticity structures to the top of the pipe. The recirculation cores generated at the top and the bottom of the cylinder are both advected in the pipe along the flow direction. The top recirculation core is attached to the interface as soon as it is generated, while the bottom one is quickly advected upwards before reaching the height of the transverse cylinder. The top recirculation core corresponds to the crest of the generated wave, while the bottom one corresponds to the wave trough. In this particular case, the velocity of advection of the vortical structures is the same as the wave velocity.

In the case of  $r = 1$  (Figure 12) recirculation cores still appear in the water phase downstream the cylinder but the interface remains almost flat. In this case, the recirculation cores tend to stay at the same horizontal level as the cylinder and are not advected towards the interface, while a jet like flow appears on top of the cylinder. The velocity computed from the cross correlation of the interface is equal to 0.42 m/s. The magnitude of velocities above and below the cylinder is higher than the wave velocity. In addition, the area occupied by the recirculation zone in the wake of the cylinder is larger than in the case shown in Figure 11. Similar results were found for the other flow rate combinations studied where  $r = 1$ .

In the cases considered here, the transitional regime defined by Sheridan et al (1997), which is characterized by an oscillation of the jet like flow adjacent to the base of the cylinder, was not observed. The Froude numbers used here, however, as well as the depths of submergence are different, while the flow is bound by the pipe wall. The vorticity field, calculated from equation 5, for the case  $Q_o=30 \text{ L min}^{-1}$  and  $Q_w=20 \text{ L min}^{-1}$  ( $r=1.5$ ,  $Fr=1.8$ ) is shown in Figure

13, where the black regions represent negative vorticity and the white regions positive vorticity. The positive vorticity cluster is localized above the cylinder and the negative one below the cylinder. These two vorticity clusters correspond to the counter rotating vortices in the wake of the cylinder. A negative vorticity cluster appears directly attached to the interface (circled in Figure 13) and seems to be in phase with the negative vorticity at the wake emitted from the bottom of the cylinder. This negative vorticity cluster attached to the interface is then advected along the pipe underneath the crest of the generated wave.

From the flow field measurements, it appears clearly that interfacial waves are actuated by the von Karman vortices while two cases can be distinguished. For low mean interface height (high flow rate ratio), the vortices attached directly to the interface and wave amplitude is increased. For high mean interface height, a jet like flow appeared on the top of the cylinder while the amplitude of the actuated waves were small.

As was discussed in section 2, the PIV experiments were carried out for the cases where the waves were linear and the interface was not very distorted. To further evaluate the effect of the cylinder on the actuation of drop formation, the two-phase flow patterns were observed with high speed imaging with and without the transverse cylinder. These studies were carried out both in the vicinity of the cylinder and at 7 m downstream. Droplet detachment was also observed as can be seen in Figure 14. However, 3D effects may still be present but cannot be quantified from these measurements.

Two mechanisms of drop generation were seen. In the first mechanism, interfacial waves are actuated by the von Karman structures shed by the cylinder and drops detach from these non-linear waves (Figure 14a). The shear in the vorticity structures close to the waves elongates the wave crests to ligaments from where the drops detach. This mechanism of droplet generation occurs when the Froude number is high or the submergence depth is low. Drops are also generated when the interface directly hits the cylinder (Figure 14b) at low depths of submergence. In this case, the interface follows the large scale structures after the cylinder and remains encapsulated at the von Karman vortex street. The small vorticity structures distort locally the interface and generate the droplets.

The flow pattern map recorded at 7 m downstream the test section inlet is shown in Figure 15, where the symbols represent the patterns with the cylinder present and the dashed line indicates the pattern transitions without the cylinder. Similar patterns were also observed a few pipe diameters after the cylinder. They are presented here at 7m to show that once drops form they persist in the flow and also to allow comparisons with flow pattern maps available in the literature where observations are carried out away from the inlet. Two patterns were

seen in the conditions investigated, stratified wavy flow (SW) and dual continuous flow (DC) where both phases are continuous but there are drops of one phase into the continuum of the other. The decrease in the depth of submergence corresponds to a move to the right hand side of the map while an increase in the Froude number corresponds to a move towards the top of the flow pattern map. The shift of the right hand boundary between SW and DC flow is therefore attributed to the effect of the von Karman structures on the interface and corresponds to the regime observed in Figure 14a. The three cases with  $r > 2.5$  represent droplet generation by direct impact of the interface on the cylinder. The PIV measurements were carried out for the cases in the stratified flow region (square points on Figure 15). The left hand side boundary is shifted with the cylinder to low mixture velocities, which indicates that the mixture velocity (or Froude number) also plays a role on drop generation.

At  $r=1$ , droplets are generated at low mixture velocities (low Froude numbers) in contrast to what is shown in Figure 12. In this particular case, a jet-like flow appeared between the upper part of the cylinder and the interface, while there were no vortices attached to the interface. It was shown by Sheridan et al (1997) that this type of flow behind the cylinder can also generate waves at the interface. It can be assumed that as the mixture velocity increases for constant flowrate ratio, the interface becomes progressively more disturbed and drops finally detach.

The cylinder can be considered as a hydrodynamic oscillator. For the range of investigated Reynolds numbers the global hydrodynamic instability generated at the wake of the cylinder prints the vortex shedding frequency to the interface. For the conditions studied this mechanism prevails over the frequencies generated at the interface at the inlet by the convective hydrodynamic instability between two fluids with different flowrates. In the current work where the cylinder diameter is constant, the actuation frequency was varied by changing the mixture velocity and the flowrate ratio. However, the results indicate a complex system. At least, in case of unbounded flows, this system involves two main different types of instabilities. At the inlet, a single shear layer between the fluids leads to a convective instability (KH instability) while a double shear layer leads to an absolute instability (vortex shedding behind the wake of the cylinder). It is believed that the wave amplitude is increased as a result of the synergy between the two types of instabilities. However, the coupling of these instabilities is not well understood, particularly for wall bounded flows and would require further work.

#### 4. Conclusions

The main objective of this study was to investigate the interactions of the wakes generated by a transverse cylinder submerged in water, with the interface in a stratified oil-water pipe flow and to actuate the transition to dispersed patterns. Velocity fields were obtained with high speed PIV in the vicinity of the cylinder. The results in single phase flow showed that the flow fields were comparable to those obtained in rectangular channels under 2D flow conditions. In two-phase flows the presence of the cylinder generated waves in the oil-water interface for high Froude numbers and low depths of cylinder submergence. The results revealed that for low depths of submergence, vorticity clusters attach to the interface and generate interfacial waves. By increasing the Froude number (i.e. the mixture velocity) these waves become increasingly non-linear.

Visual observations revealed that the presence of the cylinder changed the flow pattern map of the oil-water pipe flow. The cylinder actuated the generation of drops from the interface and reduced the transition from separated to dispersed oil-water flows to lower mixture velocities. In pipe flow, Froude number and depth of submergence are determined by the combination of the flowrates of the two phases which also define the mixture velocity and the flowrate ratio, often used as parameters in the flow pattern maps. The physical parameters which govern the flow behind the transverse cylinder are also linked to the flow pattern map.

### Acknowledgements

The project was supported by the EPSRC Programme Grant MEMPHIS. The authors would also like to acknowledge the EPSRC Instrument Pool for the loan of the high speed PIV system.

### References

- ADRIAN, R. J., & WESTERWEEL, J. 2011 Particle Image Velocimetry, *Cambridge University Press*.
- AL-WAHAIBI, T. & ANGELI, P. 2007 Transition between stratified and non-stratified horizontal oil–water flows. Part I: Stability analysis. *Chemical engineering science*, **62**, 2915-2928.
- BARNEA, D. & TAITEL, Y. 1994 Interfacial and structural stability of separated flow. *International journal of multiphase flow*, **20**, 387-414.
- BARRAL, A. H. & ANGELI, P. 2013 Interfacial characteristics of stratified liquid–liquid flows using a conductance probe. *Experiments in fluids*, **54**, 1-15.

- BARRAL, A. H. & ANGELI, P. 2013 Investigation of stratified, horizontal oil–water flow via statistical analysis of conductance probe data. *Exp. Fluids*, **54**, 1604.
- BEARMAN, P. W & ZDRAVKOVICH, M. M. 1978 Flow around a circular cylinder near a plane boundary. *Journal of Fluid Mechanics*, **89**, 33-47.
- BIRVALSKI, M., TUMMERS, M. J., DELFOS, R., HENKES, R.A.W.M. 2014 PIV measurements of waves and turbulence in stratified horizontal two-phase pipe flow. *International Journal of Multiphase Flow*, **62**, 161-173.
- BRAUNER, N. & MARON, D. M. 1991 Analysis of stratified/nonstratified transitional boundaries in horizontal gas—liquid flows. *Chemical engineering science*, **46**, 1849-1859.
- BRAUNER, N. & MARON, D. M. 1992 Flow pattern transitions in two-phase liquid-liquid flow in horizontal tubes. *International Journal of Multiphase Flow*, **18**, 123-140.
- BRAUNER, N. & MARON, D. M. 1993 The role of interfacial shear modelling in predicting the stability of stratified two-phase flow. *Chemical engineering science*, **48**, 2867-2879.
- CHARONKO, J. VLACHOS, P. Estimation of uncertainty bounds for individual particle image velocimetry measurements from cross-correlation peak ratio. *Measurement Science and Technology*, 2013, vol. 24, no 6, p. 065301.
- CHEN, J. H., PRITCHARD, W. G. & TAVENER, S. J. 1995 Bifurcation for flow past a cylinder between parallel planes. *Journal of Fluid Mechanics*, **284**, 23-41.
- CHENG, E., AHMADI, A. & CHEUNG, K. C. 2015 Measurement of the oscillatory flow field inside tapered cylindrical inkjet nozzles using micro-particle image velocimetry. *Microfluidics and Nanofluidics*, 1-12.
- CHINAUD, M., ROUMPEA, E. P., & ANGELI, P. 2015 Studies of plug formation in microchannel liquid–liquid flows using advanced particle image velocimetry techniques. *Experimental Thermal and Fluid Science*, **69**, 99-110.
- CHOI, J. H. & LEE, S. J. 2000 Ground effect of flow around an elliptic cylinder in a turbulent boundary layer. *Journal of Fluids and Structures*, **14**, 697-709.
- DIMAS, A. A. 1998 Free-surface waves generation by a fully submerged wake. *Wave motion*, **27**, 43-54.
- DING, H., SHU, C., YEO, K. S. & XU, D. 2004 Simulation of incompressible viscous flows past a circular cylinder by hybrid FD scheme and meshless least square-based finite difference method. *Computer Methods in Applied Mechanics and Engineering*, **193**, 727-744.
- DUNCAN, J. H. & DIMAS, A. A. 1996 Surface ripples due to steady breaking waves. *Journal of Fluid Mechanics*, 329, 309-339.
- EDOMWONYI-OTU, L. C. & ANGELI, P. 2015 Pressure drop and holdup predictions in horizontal oil–water flows for curved and wavy interfaces. *Chemical Engineering Research and Design*, **93**, 55-65.
- FUNADA, T. & JOSEPH, D. D. 2001 Viscous potential flow analysis of Kelvin–Helmholtz instability in a channel. *Journal of Fluid Mechanics*, **445**, 263-283.
- GRASS, A. J., RAVEN, P. W. J., STUART, R. J. & BRAY, J. A. 1984 The influence of boundary layer velocity gradients and bed proximity on vortex shedding from free spanning pipelines. *Journal of Energy Resources Technology*, **106**, 70-78.

- HU, B. & ANGELI, P. 2006 Phase Inversion and Associated Phenomena in Oil-Water Vertical Pipeline Flow. *The Canadian Journal of Chemical Engineering*, **84**, 94-107.
- HU, B., MATAR, O. K., HEWITT, G. F. & ANGELI, P. 2006 Population balance modelling of phase inversion in liquid-liquid pipeline flows. *Chemical Engineering Science*, **61**, 4994-4997.
- ISHII, M. & GROLMES, M. A. 1975 Inception criteria for droplet entrainment in two-phase concurrent film flow. *AIChE Journal*, **21**, 308-318.
- JEONG, J. & HUSSAIN, F. 1995 On the identification of a vortex. *Journal of fluid mechanics*, **285**, 69-94.
- LEI, C., CHENG, L. & KAVANAGH, K. 1999 Re-examination of the effect of a plane boundary on force and vortex shedding of a circular cylinder. *Journal of Wind Engineering and Industrial Aerodynamics*, **80**, 263-286.
- LIN, P. Y. & HANRATTY, T. J. 1987 Effect of pipe diameter on flow patterns for air-water flow in horizontal pipes. *International journal of multiphase flow*, **13**, 549-563.
- LIN, J. C. & ROCKWELL, D. 1995 Evolution of a quasi-steady breaking wave. *Journal of Fluid Mechanics*, **302**, 29-44.
- LIN, W. J., LIN, C., HSIEH, S. C. & DEY, S. 2009 Flow characteristics around a circular cylinder placed horizontally above a plane boundary. *Journal of engineering mechanics*.
- MOHAMED-KASSIM, Z. & LONGMIRE, E. K. 2004 Drop coalescence through a liquid/liquid interface. *Physics of Fluids*. **16**, 2170-2181.
- MORGAN, R. G., MARKIDES, C. N., ZADRAZIL, I. & HEWITT G. F. 2013 Characteristics of horizontal liquid-liquid flows in a circular pipe using simultaneous high-speed laser-induced fluorescence and particle velocimetry. *International Journal of Multiphase Flow*, **49**, 99-118.
- PARK, K.H, CHINAUD, M and ANGELI, P. 2016 Transition from stratified to non-stratified oil-water flows using a bluff body. *Experimental Thermal and Fluid Science*, **76**, 175-184.
- PRASAD, A. K. 2000 Stereoscopic particle image velocimetry. *Experiments in fluids*, **29**, 103-116.
- KUMARA, W.A.S; ELSETH, G; HALVORSEN, B.M and MELAAEN, M.C, 2010, Comparison of Particle Image Velocimetry and Laser Doppler Anemometry measurement methods applied to the oil-water flow in horizontal pipe, *Flow Measurement and Instrumentation* **21**, Issue 2, 105-117.
- RAFFEL, M, WILLERT, C. E., WERELEY, S., et al. Particle image velocimetry: a practical guide. Springer, 2013.
- REICHL, P., HOURIGAN, K. & THOMPSON, M. C. 2005 Flow past a cylinder close to a free surface. *Journal of Fluid Mechanics*, **533**, 269-296.
- SCIACCHITANO, A, WIENEKE, B, et SCARANO, F. PIV uncertainty quantification by image matching. *Measurement Science and Technology*, 2013, vol. 24, no 4, p. 045302.
- SHERIDAN, J., LIN, J. C. & ROCKWELL, D. 1997 Flow past a cylinder close to a free surface. *Journal of Fluid Mechanics*, **330**, 1-30.
- SCHLICHTING H. 1955 Boundary-layer theory. *McGraw-Hill*.

- SIMMONS, M. J. H. & AZZOPARDI, B. J. 2001 Drop size distributions in dispersed liquid–liquid pipe flow. *International journal of multiphase flow*, **27**, 843-859.
- STANISLAS, M., OKAMOTO, K., KÄHLER, C. J., WESTERWEEL, J. & SCARANO, F. 2008 Main results of the third international PIV challenge. *Experiments in Fluids*, **45**, 27-71.
- TAITEL, Y. & DUKLER, A. E. 1976 A model for predicting flow regime transitions in horizontal and near horizontal gas-liquid flow. *AIChE Journal*, **22**, 47-55.
- TAITEL, Y. & BARNEA, D. 1990 A consistent approach for calculating pressure drop in inclined slug flow. *Chemical engineering science*, **45**, 1199-1206.
- THEUNISSEN, R., SCARANO, F. & RIETHMULLER, M. L. 2008 On improvement of PIV image interrogation near stationary interfaces. *Experiments in Fluids*, **45**, 557-572.
- TRIANTAFYLLOU, G. S. & DIMAS, A. A. 1989 Interaction of two-dimensional separated flows with a free surface at low Froude numbers. *Physics of Fluids A: Fluid Dynamics*, **1**, 1813-1821.
- WANG, X. K. & TAN, S. K. 2008 Near-wake flow characteristics of a circular cylinder close to a wall. *Journal of Fluids and Structures*, **24**, 605-627.
- WANG, X. K. & TAN, S. K. 2008 Comparison of flow patterns in the near wake of a circular cylinder and a square cylinder placed near a plane wall. *Ocean Engineering*, **35**, 458-472.
- WIENEKE, B. PIV uncertainty quantification from correlation statistics. *Measurement Science and Technology*, 2015, vol. 26, no 7, p. 074002.
- ZHOU, B., WANG, X., GUO, W., ZHENG, J. & TAN, S. K. 2015 Experimental measurements of the drag force and the near-wake flow patterns of a longitudinally grooved cylinder. *Journal of Wind Engineering and Industrial Aerodynamics*, **145**, 30-41.
- ZOVATTO, L. & PEDRIZZETTI, G. 2001 Flow about a circular cylinder between parallel walls. *Journal of Fluid Mechanics*, **440**, 1-25.

**Table**

	Water	Exxsol D140	$Re_{pipe}$	$Re_{cyl}$
Density ( $kg/m^3$ )	1000	830		
Discosity (cP)	1	5.5		
	Flow rate (L/min)	Flow rate (L/min)		
Single phase experiments	20		11 471	1550
	25		14 338	1938
	30		17 206	2325
	35		20 074	2713
	40		22 941	3100
	45		25 809	3488
Two phase experiments	20	20	22 941	3100
	20	25	25808	3487
	20	30	28676	3875
	25	20	25808	3487
	25	25	28676	3875
	25	30	31544	4262

**Table 1:** Summary of experimental conditions

## Figures

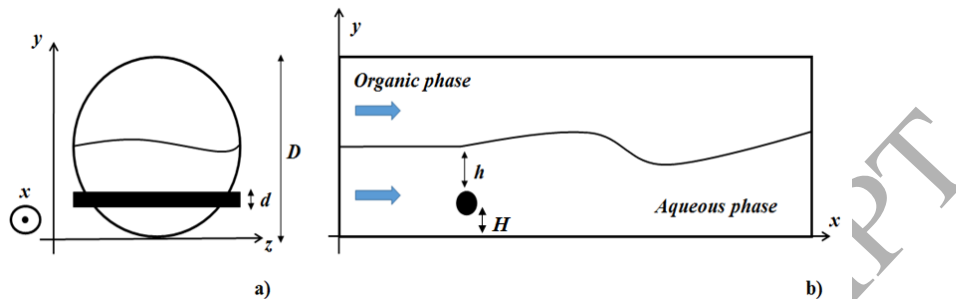


**Figure 1:** Schematic of the pipe section with the transverse cylinder. a) Axial view and (b) side view.

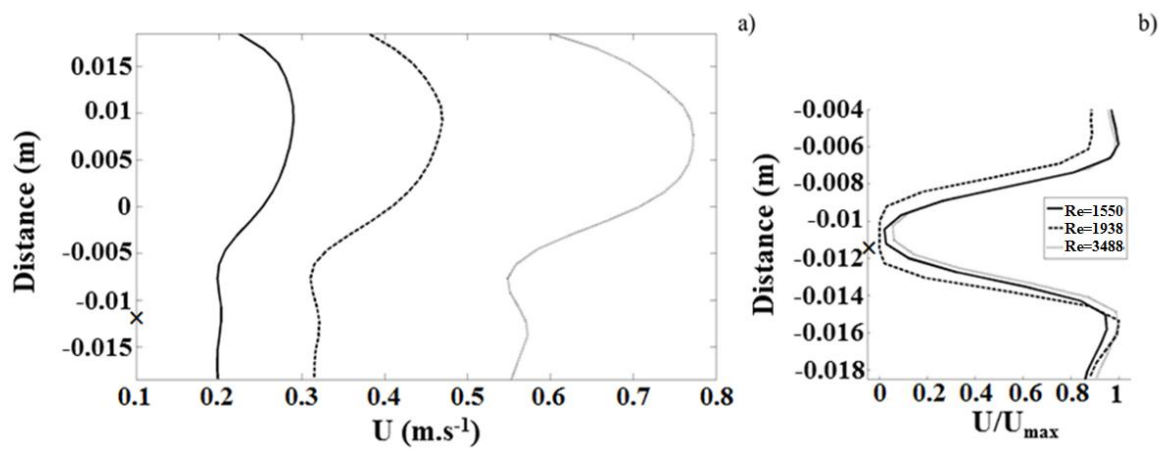


**Figure 2:** Time averaged axial velocity profiles in single phase flow. The velocity profiles have been averaged over axial distance a) from  $3d$  to  $14d$  and b) from  $0$  to  $2d$ . The  $x$  indicates the position of the bottom of the rod.

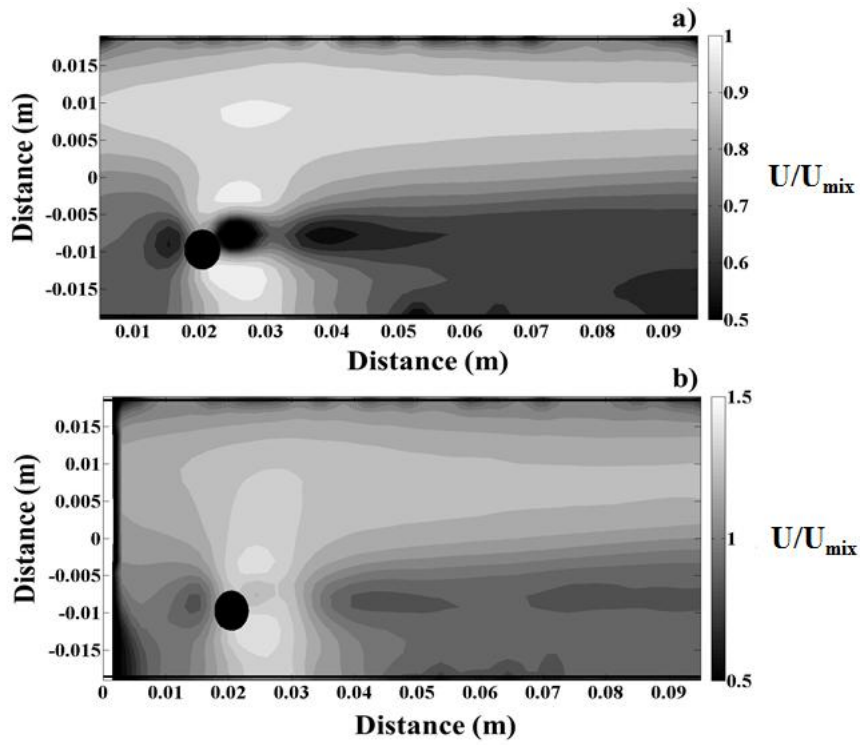


**Figure 3:** Time averaged axial velocity map for single phase flow and Reynolds numbers a) 1550 and b) 3488. The axial velocity has been normalized by the corresponding  $U_{mix}$ .

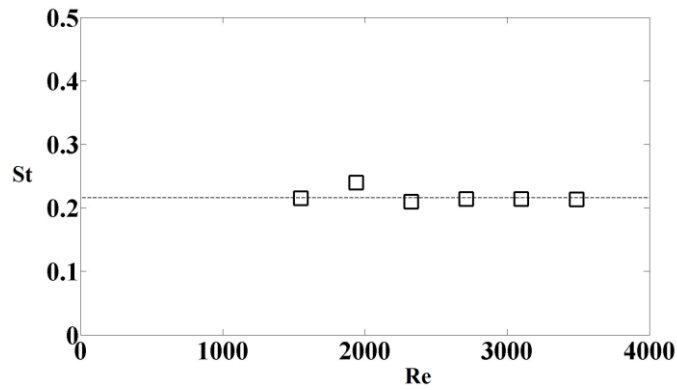


**Figure 4:** Strouhal number plotted against Reynolds number in single phase flow. The linear fit shows a constant value  $St=0.216 \pm 0.010$ .

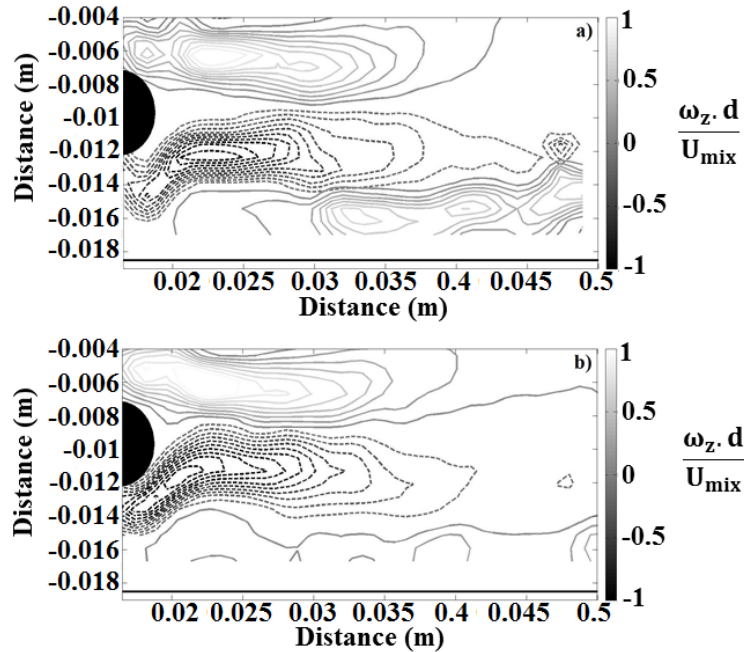


**Figure 5:** Time averaged spanwise vorticity over distance from cylinder for a)  $Re=1550$  and b)  $Re=3488$ . The solid lines correspond to positive regions while the dashed lines correspond to negative regions.

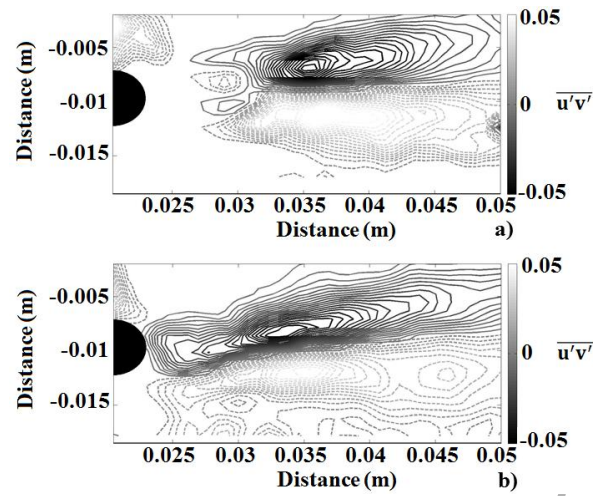


**Figure 6:** Time averaged Reynolds stresses over distance from cylinder for a)  $Re=1550$  and b)  $Re=3488$ . The solid lines correspond to the negative region while the dashed lines correspond to the positive region.

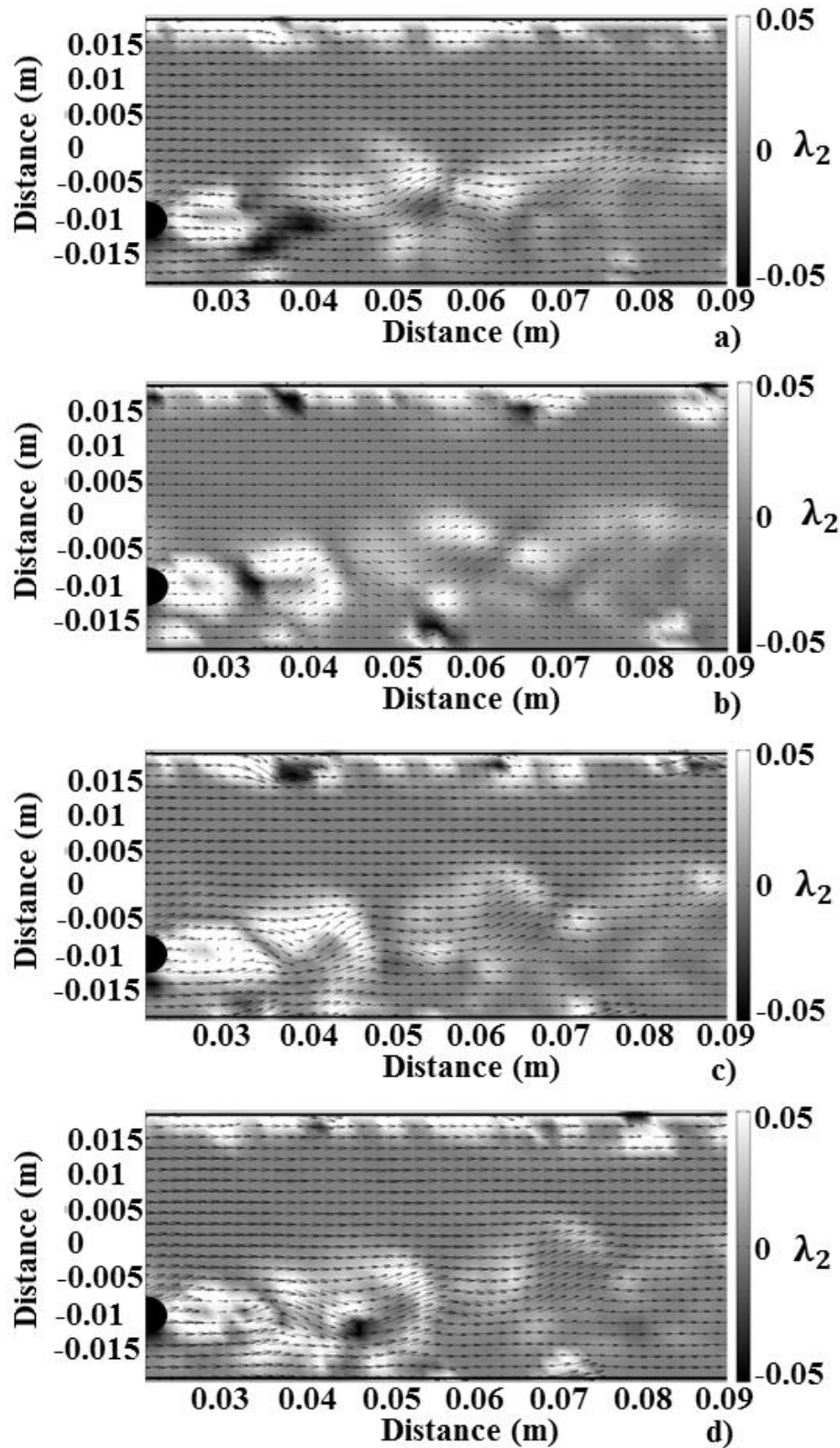


**Figure 7:** Change of parameter  $\lambda_2$  over time for  $Re=1550$ . Velocity field has been superimposed. The time delay between each image is 20 ms.

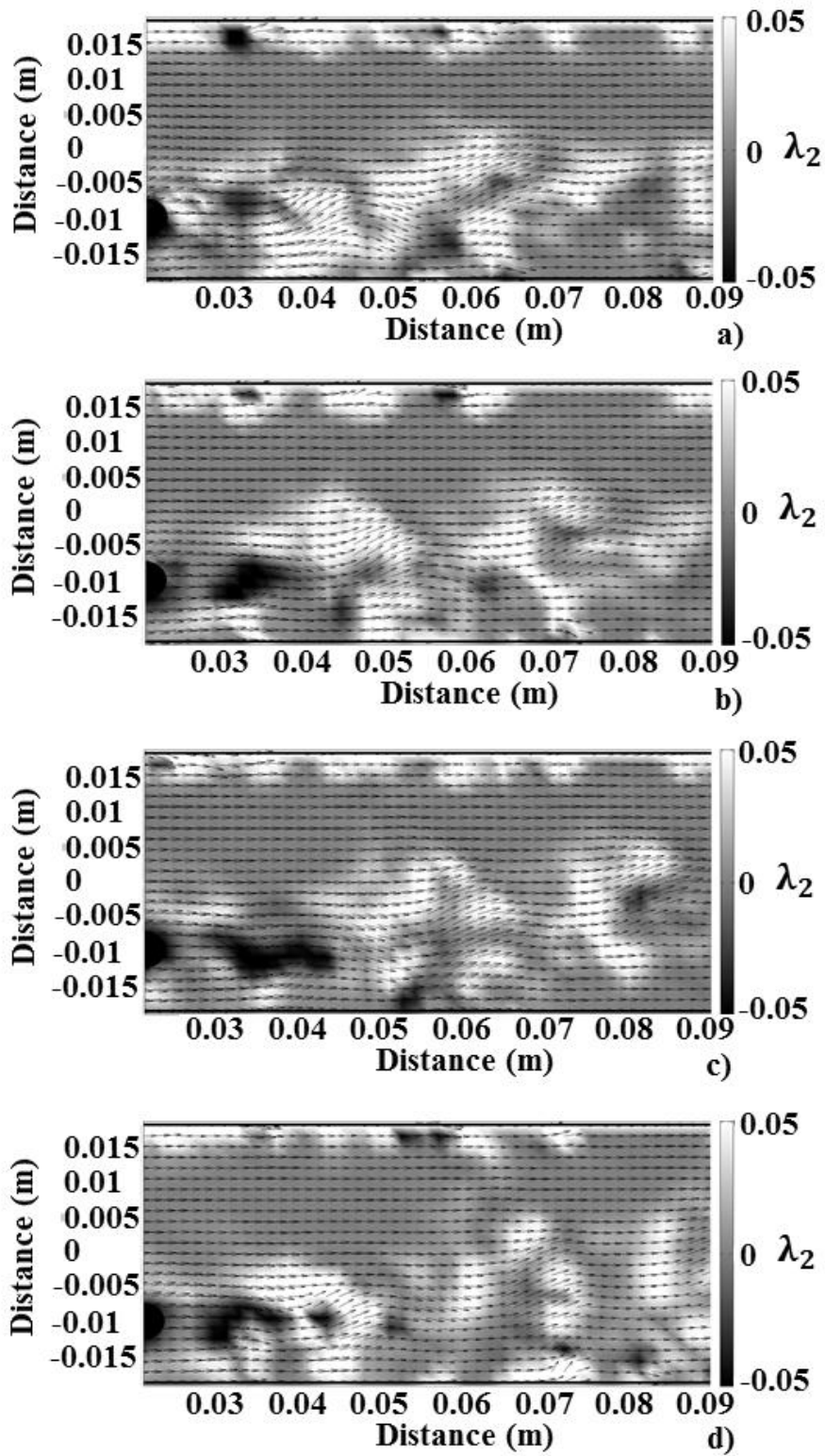


**Figure 8:** Change of parameter  $\lambda_2$  over time for  $Re=3488$ . Velocity field has been superimposed. The time delay between each image is 10 ms.

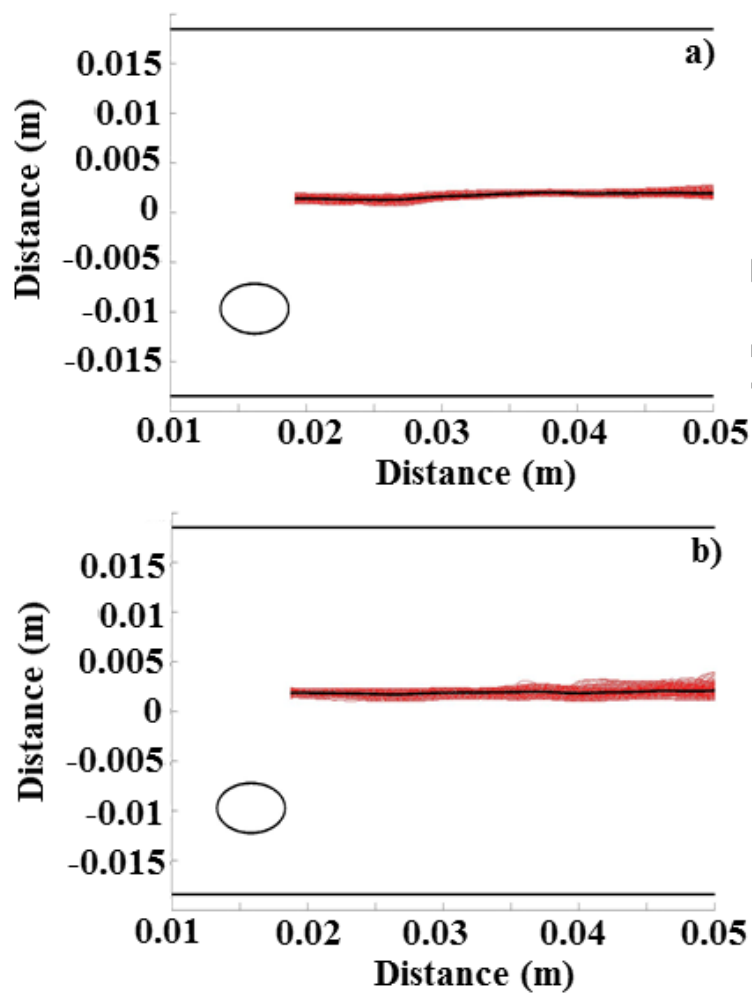


**Figure 9:** Interface shape for  $r=1$  and a)  $Fr=1.4$ , b)  $Fr=1.8$ . The time averaged interface shape (solid thick line) has been superimposed to 200 interface shapes obtained over time (solid thin lines)

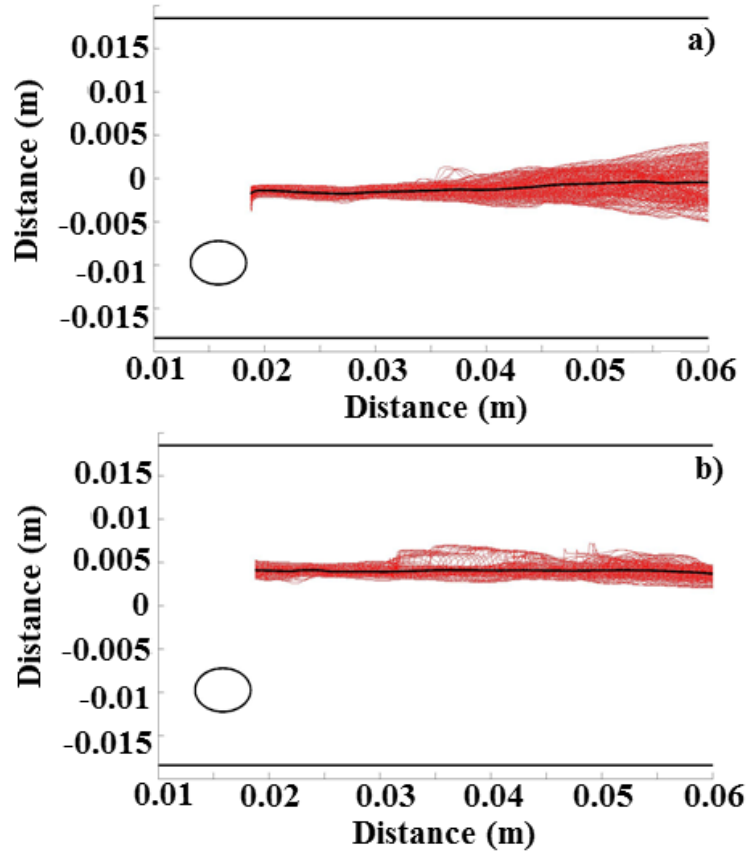


**Figure 10:** Interface shape for  $Fr=1.8$  and a)  $r=1.5$  and b)  $r = 0.66$ . The time averaged interface shape (solid thick line) has been superimposed to 200 interface shapes obtained over time (solid thin lines).

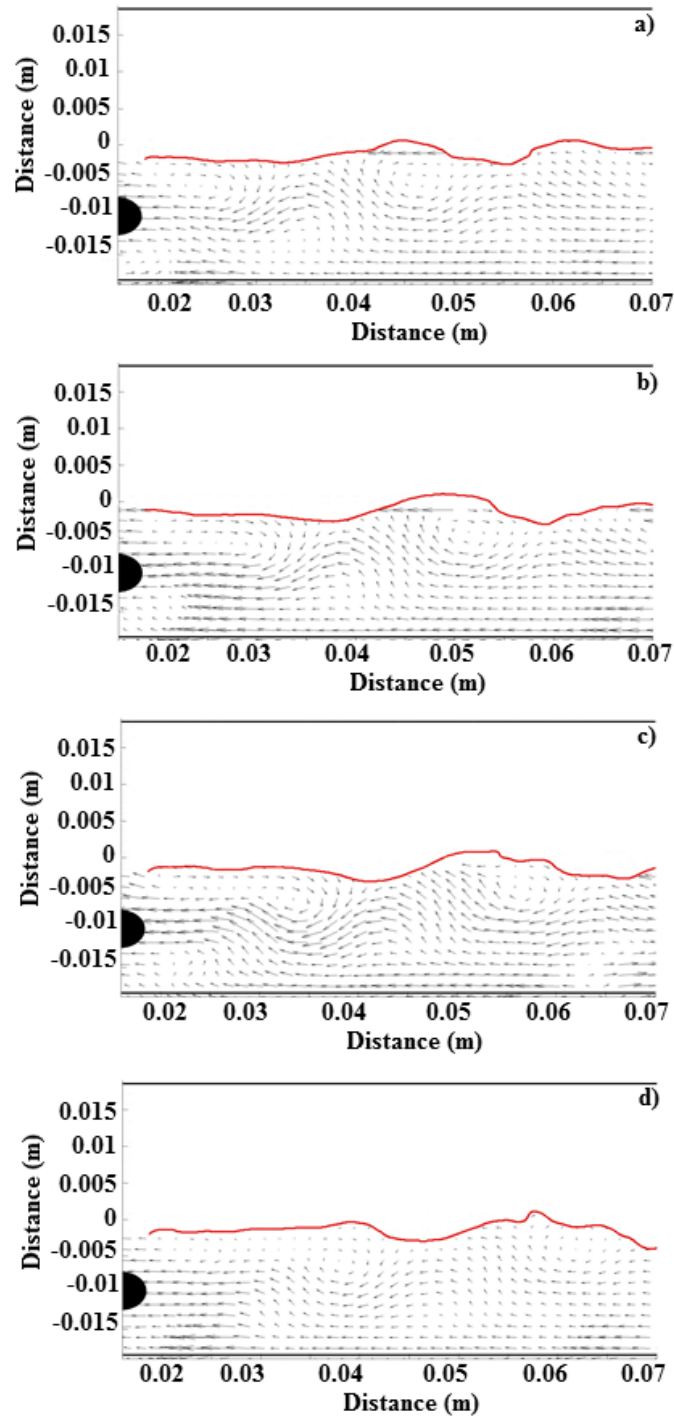


**Figure 11:** Time sequence of the velocity field after the cylinder with the mean wave velocity ( $0.8 \text{ m/s}$ ) subtracted.  $Q_0=30 \text{ L}\cdot\text{min}^{-1}$  and  $Q_w=20 \text{ L}\cdot\text{min}^{-1}$  ( $r=1.5$ ,  $Fr=1.8$ ). The time delay between images is  $6.7 \text{ ms}$ .

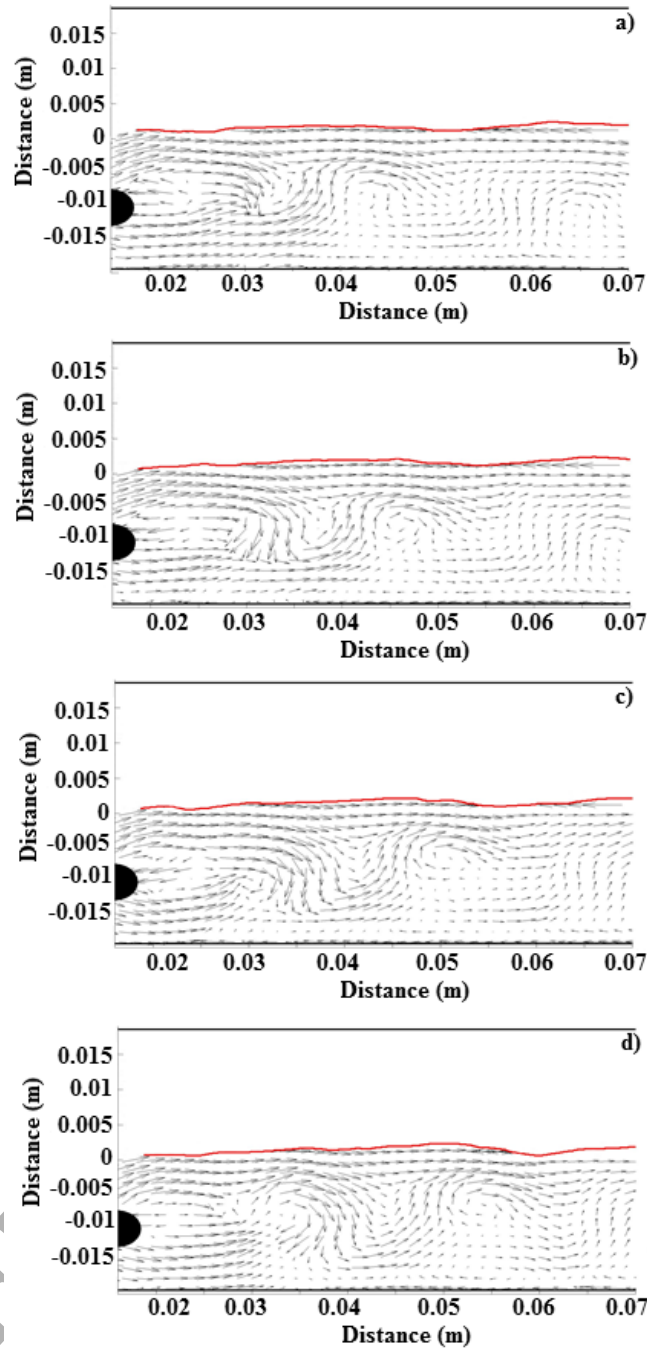


**Figure 12:** Time sequence of the velocity field after the cylinder with the mean wave velocity (0.4 m/s) subtracted.  $Q_o=20 \text{ L}\cdot\text{min}^{-1}$  and  $Q_w=20 \text{ L}\cdot\text{min}^{-1}$  ( $r=1$ ,  $Fr=1.4$ ). The time delay between images is 6.7 ms.

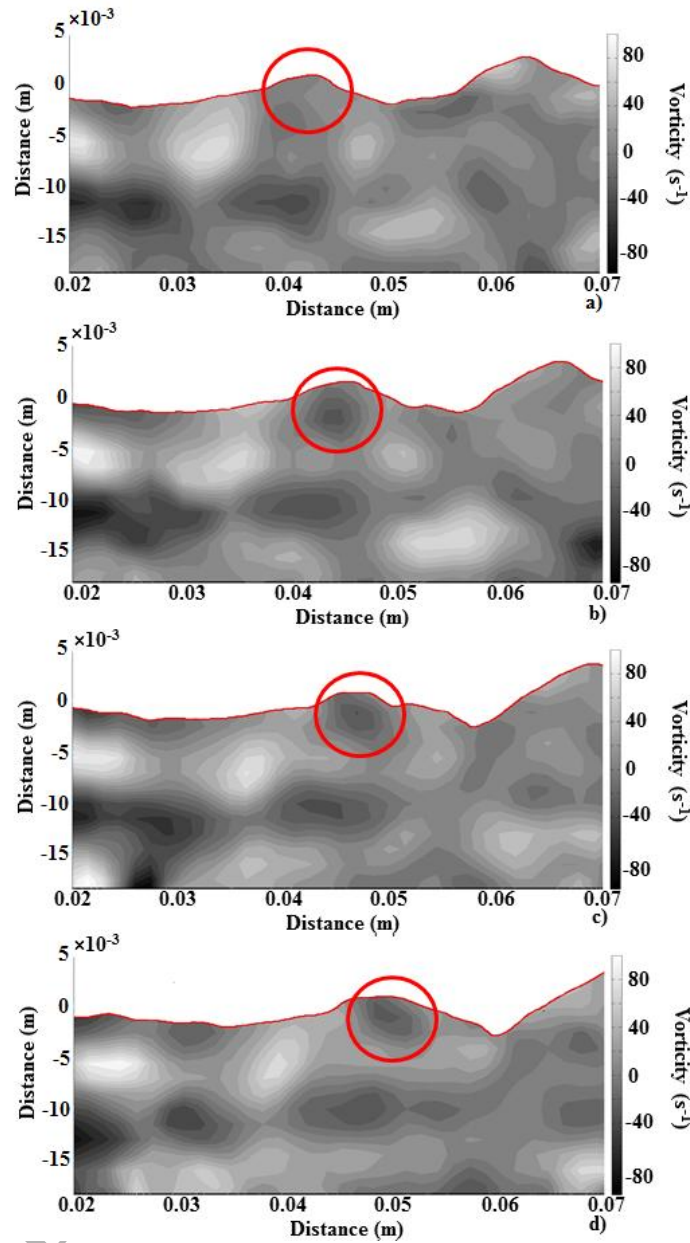


**Figure 13:** Time sequence of the vorticity field after the cylinder for  $Q_o=30 \text{ L}\cdot\text{min}^{-1}$  and  $Q_w=20 \text{ L}\cdot\text{min}^{-1}$  ( $r=1.5$ ,  $Fr=1.8$ ). The time delay between images is 6.7 ms. The circles show the negative vorticity cluster attached to the interface.

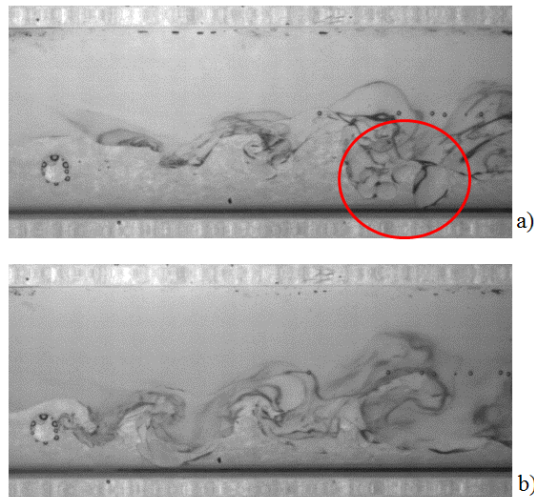


**Figure 14:** Droplet generation for a)  $U_{mix}=0.93$  m/s and  $r=2$  and b)  $U_{mix}=1.09$  m/s and  $r=2.5$ . The circle in a) indicates the position of the ligament which will lead to droplet detachment.

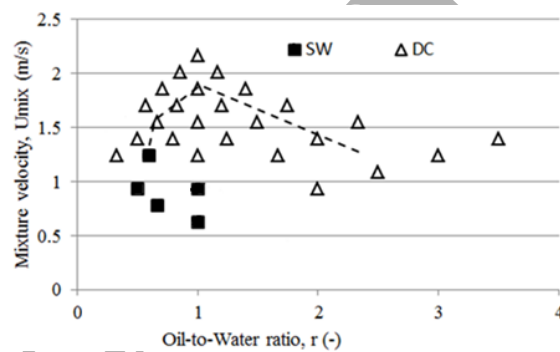


**Figure 15:** Flow pattern map (symbols) with the cylinder, 7 m downstream the inlet. The dashed line corresponds to the boundary between stratified wavy (SW) and dual continuous (DC) patterns without the cylinder.